Pulsed-Laser Deposited $Pb(Zr_{0.52},Ti_{0.48})O_3$-on-Silicon Resonators with High-Stopband Rejection Using Feed-Through Cancellation

H. Yagubizade,[1, a)] M. Darvishi,[1] Y.-Y. Chen,[2, b)] M.D. Nguyen,[1, 3, 4] J.M. Dekkers,[1, 3] R.J. Wiegerink,[1] M.C. Elwenspoek,[1] and N.R. Tas[1]

[1)] *MESA$^+$ Institute for Nanotechnology, University of Twente, Enschede, The Netherlands*

[2)] *Department of Mechanical Engineering, Tatung University, Taipei, Taiwan*

[3)] *SolMateS BV, Enschede, The Netherlands*

[4)] *International Training Institute for Materials Science (ITIMS), Hanoi University of Science and Technology, Hanoi, Vietnam*

(Dated: 4 February 2013)

A length extensional mode lead zirconate titanate (PZT)-on-Si resonator is presented using 50 Ω termination with high-stopband rejection exploiting feed-through cancellation. A 250 nm-thick (100)-dominant oriented PZT thin-film deposited on top of 3 µm Si using pulsed laser deposition (PLD) has been employed. The resonator is presented with the length of 40 µm (half-wavelength), which corresponds to a resonance frequency of about 83 MHz. The effect of feed-through cancellation has been studied to obtain high-stopband rejection using bottom electrode patterning in the presence of a specific grounding resistance. Using this technique, the stopband rejection can be improved by more than 20 dB.

Nowadays, there is a great demand for integrated and reconfigurable RF bandpass filters to get rid of bulky, off-chip and expensive SAW filters and resonators, which can reduce the form factor, cost and increase the functionality of the next generation of wireless devices. Radio frequency MEMS (RF-MEMS) resonators are promising candidates for this purpose. Lamb-wave piezoelectric RF-MEMS resonators have demonstrated promising performance, such as low motional impedance and high Q-factor[1–5]. Their Q-factor has been boosted by integrating them with single crystalline materials, e.g. single-crystalline silicon[1,2] and silicon carbide[3,4], which store energy and deliver it back in each cycle with less loss compared to the piezoelectric medium. Also Lamb-wave resonators are of great interest for highly sensitive sensors due to their high Q-factor[5].

AlN, ZnO and recently PZT thin-films are the prevalent piezoelectric materials utilized in the resonators. Of these, PZT has the highest electromechanical coupling-factor. Also, the ferroelectric properties of PZT makes it more attractive for RF-MEMS applications. On the other hand, PZT has a lower phase velocity, which makes it difficult to achieve very-high resonance frequencies. However, higher composite phase velocities can be obtained by PZT in combination with other materials having higher phase velocities (e.g. silicon)[6]. Previously, PZT has been grown using chemical solution deposition methods[7] for RF-MEMS applications. In this paper, a pulsed laser deposition (PLD)[8] has been exploited to grow a high-quality PZT thin-film with (100)-dominant orientation for RF-MEMS application. PZT suffers from a high feed-through due to its high dielectric permittivity and, as a consequence, drastically reduces the stopband rejection[9,10]. In this paper, we propose a feed-through cancellation method in the presence of specific grounding resistances (non-zero grounding) in input- and output-sides, which always exist and prevent the perfect grounding. Particularly, these grounding resistances have to be considered in the design of high-dielectric resonators, such as PZT.

In this paper, a length extensional mode resonator, Fig. 1(a), with the length of 40 µm (half-wavelength) is presented. The basic configurations are presented in Fig. 1(b) and Fig. 1(c). The key aspects set forth in this paper are the use of PLD-based PZT thin-film with its characteristics in RF-MEMS as well as presenting a feed-through cancellation method, which improves the stopband rejection by more than 20 dB.

The effect of non-zero ground resistance R_g on the performance of a 2-port resonator with and without a patterned bottom-electrode is explored. An electrical model of a two-port resonator without bottom-electrode patterning is illustrated in Fig. 2(a)[9,10]. The filter shown in Fig. 2(a) can be simplified to Fig. 2(b), because of the high impedance level of the resonator for frequencies out of its passband. The stopband gain of the resonator can be inferred from the circuit shown in Fig. 2(b). As R_g increases, the voltage gain at node V_x increases and as a consequence the rejection floor of the 2-port resonator can rise considerably and lower the stopband rejection to less than typically 5 dB. The stopband gain of the resonator A_{sb} in terms of $r = R_g/R_s$ and $\tau = R_s C_0$ can be described as:

$$A_{sb} = 20\log\left(\frac{0.5r\tau^2\omega_0^2}{\sqrt{\left(1-(1+r)\,\tau^2\omega_0^2\right)^2+\tau^2\omega_0^2\,(2+r)^2}}\right) \quad (1)$$

The parasitic path in Fig. 2(a), is also responsible for the reduction of the passband gain of the resonator. By assuming that the source and load impedance are much lower than the motional impedance of the the resonator,

[a)] Electronic mail: h.yagubizade@utwente.nl

[b)] Electronic mail: yychen@ttu.edu.tw

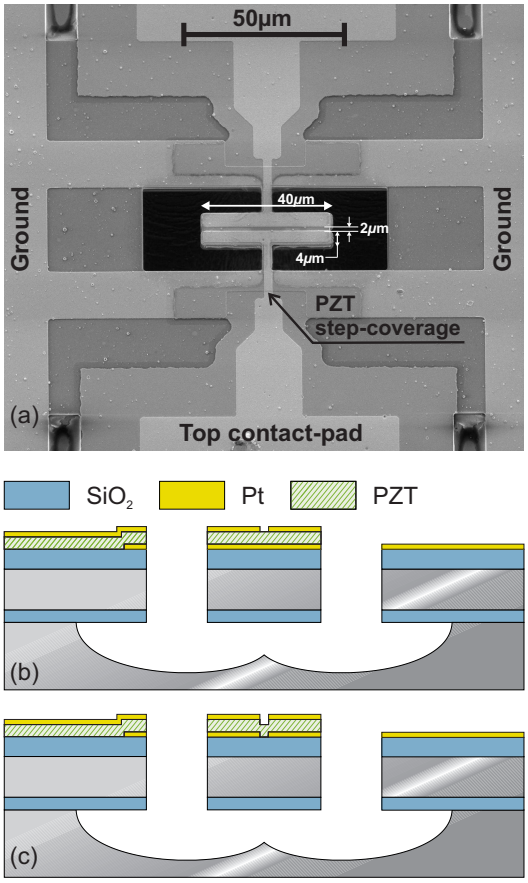

FIG. 1. (a) Scanning electron micrograph (SEM) of a PZT-on-silicon resonator with the size of $10 \times 40\,\mu m^2$. (b) The cross-section schematic of the un-patterned bottom-electrode device. (c) The cross-section schematic of the patterned bottom-electrode device.

Fig. 2(a) can be simplified to Fig. 3 for frequencies around its resonance frequency. It can be shown that the current through the parasitic path has approximately 180° phase difference relative to the current through the resonator and consequently leads to a reduction in the total current delivered to the load resistance. The phase of V_x is approximately 90° larger than the phase of V_{in}, if $C_0 R_g \omega_0 << 1$, because of the highpass filtering between node V_x and V_{in}. Also, the phase of I_{par} is 90° larger than the phase of V_x and therefore, I_{par} is anti-phase with V_{in}. On the other hand, I_{res} is in-phase with V_{in}. Therefore, I_{res} and I_{par} will be anti-phase (see Fig. 3).

The effect of parasitic ground resistance on the transfer function of the resonator can be mitigated by splitting the ground connections of the input- and output-ports as shown in Fig. 2(c). As seen, the resonator is actuated by the voltage across C_0 which is modified compared to the model presented by Pulskamp et al.[10]. In this way, the sensitivity of the transfer function of the filter to the non-zero ground resistance R_g will be drastically reduced. Using this technique, the parasitic path through the parasitic ground resistance will be eliminated.

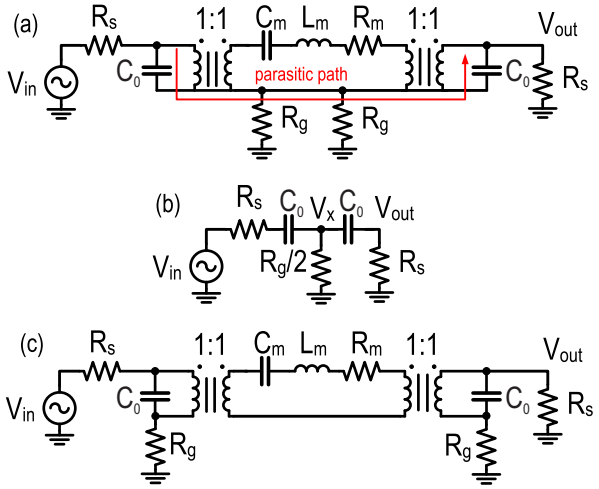

FIG. 2. (a) A conventional 2-port resonator, including the static capacitance of the resonator, C_0, motional capacitance, C_m, inductance, L_m, and impedance, R_m, and the termination impedances, R_s. (b) Simplified model of the conventional 2-port resonator for frequencies outside the passband of the resonator (c) Splitting the ground of input- and output-ports to eliminate the parasitic path due to non-zero parasitic ground resistances, R_g.

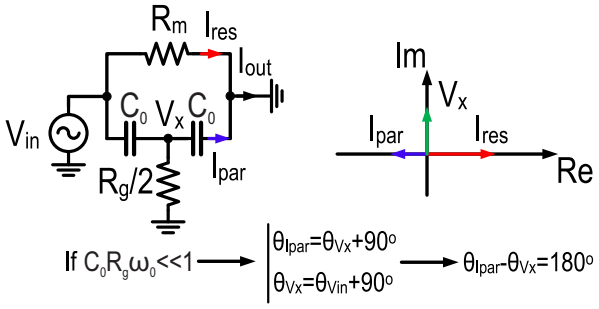

FIG. 3. The simplified configuration of a conventional 2-port resonator at its resonance frequency.

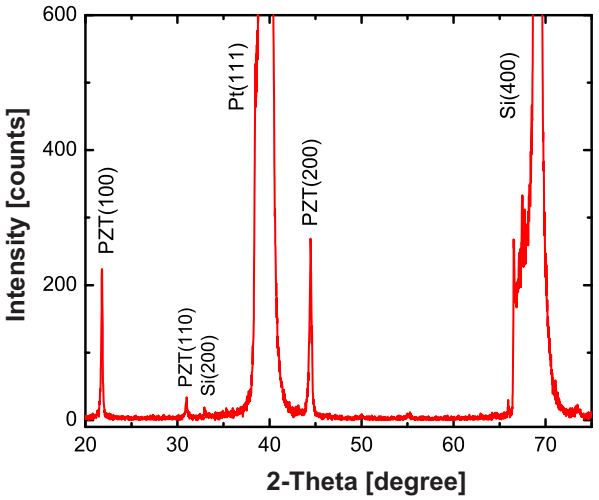

FIG. 4. XRD pattern of PZT thin-films on $Pt/Ti/SiO_2/Si$ wafers.

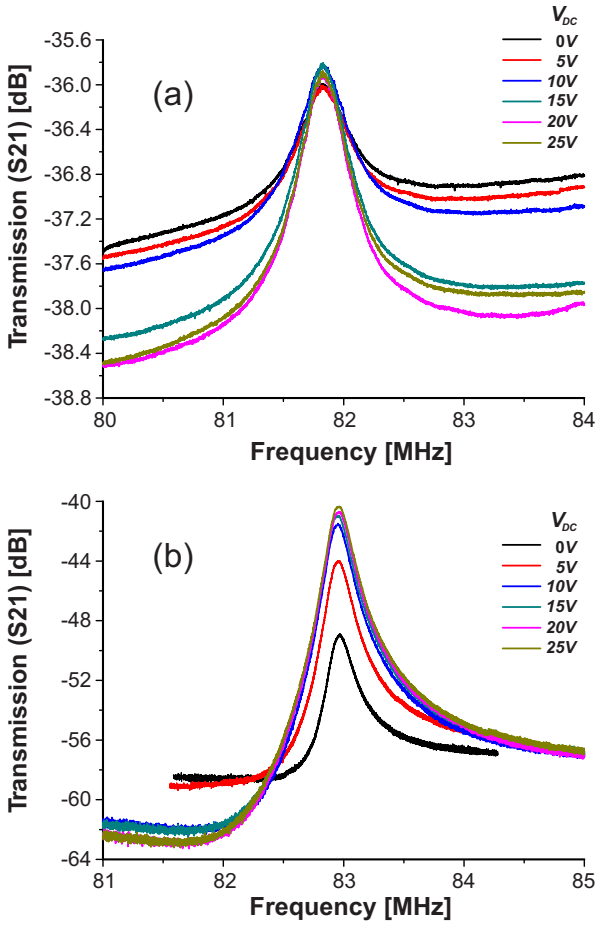

FIG. 5. Measured transmission gain of resonators using 50 Ω termination (a) with un-patterned bottom-electrode, (b) with patterned bottom-electrode.

The fabricated devices are shown in Fig. 1. In the 5-mask fabrication process, the bottom-electrode has been patterned before growing the PZT. The devices have been fabricated in a 3 µm silicon-on-insulator (SOI) wafer with 0.5 µm buried oxide (BOX) layer. During the first step, a 670 nm silicon-oxide layer was grown. The thickness of this layer is chosen to compensate the residual stresses of the other layers in the stack. 10/100 nm Ti/Pt has been sputtered and patterned using the first mask. A (100)-dominant thin-film (250 nm) PZT has been grown using PLD on $LaNiO_3$ as a seed layer. The crystalline structure of the PZT thin-films was measured using a Philips XPert X-ray diffractometer (XRD). A typical XRD pattern of the optimized PZT thin-films grown on 4-inch $Pt/Ti/SiO_2/Si$ wafers, using large-scale PLD, is given in Fig. 4. The films were prepared at 600 °C with an oxygen pressure of 0.1 mbar. The θ–2θ scan clearly indicates the growth of PZT thin-films with (100)-preferred orientation and no pyrochlore phase is observed. On top of PZT, 100 nm thick Pt has been sputtered. Using the second mask, the top Pt layer has been patterned, followed by patterning PZT using a wet etchant (the third mask). Around the devices, an area has been opened by reactive ion etching (RIE) of the $SiO_2/Si/SiO_2$ layer stack (fourth mask). Finally, using the fifth mask, the devices were released by isotropic etching of silicon, while the silicon device layer was protected by photoresist. In this fabrication process, the bottom Pt layer was etched under the top Pt contact-pads to minimize the parasitic capacitances. As seen in Fig. 1(a), PZT step-coverage has isolated the top and bottom Pt layers to prevent the shortcut.

The resonators were characterized in an RF probe station using GSG probes. A SOLT calibration has been performed using impedance standard substrates (ISSs). All the measurements have been done by applying 0 dBm input power. The grounding resistances of all the measured devices are $R_g \approx 5\,\Omega$. The frequency response of the fabricated devices for different DC-bias voltages are shown in Fig. 5. The DC-bias voltage has been applied both at the input- and output-ports using Bias-T's for all measurements. The frequency response of the un-patterned and patterned bottom-electrode, is shown in Fig. 5(a) and Fig. 5(b), respectively. It demonstrates clearly the effectiveness of bottom-electrode patterning on enhancing the stopband rejection. Thus, by utilizing this technique, the stopband rejection can be improved by more than 20 dB.

The motional impedance of the resonator at different DC-bias voltages considering R_g as well as C_0 has been extracted using Eq. (2), assuming that $R_m >> R_s$.

$$S_{21}[\mathrm{dB}] = -20\log\left(1+(R_g+R_s)^2\,C_0^2\omega_0^2\right) - 20\log\left(1+\frac{R_g}{R_s}\right) - 20\log\left(1+\frac{R_m}{2R_s}\right) \qquad (2)$$

On the other hand, using the mechanical properties of a piezoelectric-transduced resonator, the motional impedance of fundamental length extensional mode can be calculated as[1,2,6]

$$R_m = \frac{\pi}{4}\frac{{\rho_{eff}}^{0.5}{E_{eff}}^{0.5}}{Q}\frac{t_{total}}{W}\frac{1}{{e_{31}}^2}. \qquad (3)$$

In Eq. (3), t_{total} is the total device composite stack thickness ($t_{total} = t_{BOX} + t_{Si} + t_{SiO_2} + t_{Pt,bottom} + t_{PZT} + t_{Pt,top}$). The width of each input- and output-electrode

TABLE I. Material constants used in the calculations.[11]

	Si<110>	SiO_2	Pt	PZT
E [GPa]	168.9	70	137.9	95.2
ρ [kg/m^3]	2329	2200	21090	7500
ν	0.064	0.17	0.25	0.35

TABLE II. The patterned bottom-electrode resonator's performance at different DC-bias voltages.

DC-bias[V]	f_{res}[MHz]	Q-factor	C_m[fF]	L_m[mH]	R_m[kΩ]	e_{31} [a] [C/m^2]
0	82.9694	354	0.20	18.73	27.5	-1.420
5	82.9542	382	0.32	11.39	15.5	-1.821
10	82.9524	400	0.41	8.88	11.5	-2.062
15	82.9524	393	0.45	8.17	10.8	-2.150
20	82.9620	393	0.46	7.94	10.5	-2.181
25	82.9620	392	0.48	7.60	10.1	-2.229

[a] Other possible involved transductions, like capacitive, are neglected in these calculations.

is W_e=4 µm with 2 µm spacing in between, illustrated in Fig. 1(a). The total width of the resonator is W=10 µm. The values for the Young's moduli (E_i), densities (ρ_i) and Poisson's ratios (ν_i) are listed in Table I.

By comparing the measured (Eq. (2)) and calculated (Eq. (3)) motional impedances, the transverse piezoelectric coefficient (e_{31}) of 250 nm-thick PZT has been extracted at different DC-bias voltages and listed in Table II. It is illustrated that the absolute value of the e_{31} increased from 1.420 to 2.229 C/m^2 with DC-bias voltage in the range of 0-25 V. The variation of the e_{31} with the DC-bias voltage is associated with the piezoelectric domain re-orientation process. At low DC-bias voltages (0-10 V), the main contribution to the e_{31} is due to the increase in the domain reversal with increasing DC-bias voltage. At higher DC-bias voltages (15-25 V), most switchable domains have already been aligned along the direction of the DC-bias voltage, the e_{31} variation is smaller since it is determined mainly by the variations of the dipoles[12].

By applying the DC-bias voltage, the motional impedance is decreasing due to the enhancing of the transverse piezoelectric coefficient. Therefore, as seen in Fig. 5(b), by applying the DC-bias voltage, the passband gain of the resonator increases. The motional capacitance (C_m) and inductance (L_m) have been extracted and reported in Table II.

At higher DC-bias voltages, the resonator's efficiency increases, but the corresponding increase in effective Young's modulus will lead to a shift in resonance frequency. As the PZT thin-film fabricated in this paper is only 250 nm thick, the shift in resonance frequency is considerably lower than the one in previous designs[1], leading to a measured frequency shift of only 0.03%.

In conclusion, we demonstrated a feed-through cancellation method to improve the stopband rejection of PZT-on-Si resonator based on bottom-electrode patterning only. We have used a high-quality PLD-based PZT thin-film. Using the proposed technique, the stopband rejection of the resonator has been improved by more than 20 dB.

The authors would like to thank Meint de Boer and Erwin Berenschot for helping in fabrication and prof. Guus Rijnders for helpful discussions and sharing his expertise on PLD-based PZT thin-film. This work is carried out within the CREAM project of STW, Dutch Technology Foundation, the Netherlands.

[1] H. Chandrahalim, S. Bhave, R. Polcawich, J. Pulskamp, D. Judy, R. Kaul and M. Dubey, Appl. Phys. Lett. **93** 233504 (2008).
[2] G. K. Ho, R. Abdolvand, A. Sivapurapu, S. Humad, and F. Ayazi, J. Microelectromech. Syst. **17**, 512 (2008).
[3] C.-M. Lin, Y.-Y. Chen, V.V. Felmetsger, D.G. Senesky and A.P. Pisano, Adv. Mater. **24**, 2722-2727 (2012).
[4] S. Gong, N.-K. Kuo G. Piazza, J. Microelectromech. Syst. **21**, 253-255 (2012).
[5] T. Manzaneque, V. Ruiz, J. Hernando-Garnia, A. Ababneh, H. Seidel and J.L. Sanchez-Rojas, Appl. Phys. Lett. **101** 151904 (2012).
[6] H. Chandrahalim, S. Bhave, R. Polcawich, J. Pulskamp and R. Kaul, IEEE Trans. Ultrason. Ferroelectr. Freq. Control **57** 2035-2041 (2010).
[7] G.L. Smith, J.S. Pulskamp, L.M. Sanchez, D.M. Potrepka, R.M. Proie, T.G. Ivanov, R.Q. Rudy, W.D. Nothwang, S.S. Bedair, C.D. Meyer and R.G. Polcawich, J. Am. Ceram. Soc. **95** 1-16 (2012).
[8] M.D. Nguyen, M. Dekkers, E. Houwman, R. Steenwelle, X. Wan, A. Roelofs, T. Schmitz-Kempen and G. Rijnders, Appl. Phys. Lett. **99** 252904 (2011).
[9] S.S. Bedair, D. Judy, J. Pulskamp, R.G. Polcawich, A. Gillon, E. Hwang and S. Bhave, Appl. Phys. Lett. **99** 103509 (2011).
[10] J.S. Pulskamp, S.S. Bedair, R.G. Polcawich, D. Judy and S. Bhave, IEEE Frequency Control Symposium, San Fransisco, CA, 2011.
[11] M. Dekkers, H. Boschker, M van Zalk, M. Nguyen, H. Nazeer, E. Houwman and G. Rijnders, J. Micromech. Microeng. **23** 025008 (2013).
[12] C. Ayela, L. Nicu, C. Soyer, E. Cattan, and C. Bergaud, J. Appl. Phys. **100**, 054908 (2006).